

# Topological Triply Degenerate Points Induced by Spin-Tensor-Momentum Couplings

Haiping Hu, Junpeng Hou, Fan Zhang, and Chuanwei Zhang\*

*Department of Physics, The University of Texas at Dallas, Richardson, Texas 75080, USA*

The recent discovery of triply degenerate points (TDPs) in topological materials has opened a new perspective toward the realization of novel quasiparticles without counterparts in quantum field theory. The emergence of such protected nodes is often attributed to spin-vector-momentum couplings. Here we show that the interplay between spin-tensor- and spin-vector-momentum couplings can induce three types of TDPs, classified by different monopole charges ( $\mathcal{C} = \pm 2, \pm 1, 0$ ). A Zeeman field can lift them into Weyl points with distinct numbers and charges. Different TDPs of the same type are connected by intriguing Fermi arcs at surfaces, and transitions between different types are accompanied by level crossings along high-symmetry lines. We further propose an experimental scheme to realize such TDPs in cold-atom optical lattices. Our results provide a framework for studying spin-tensor-momentum coupling-induced TDPs and other exotic quasiparticles.

*Introduction.*—Topological states of matter [1, 2] provide a fertile ground for discovering new quasiparticles in condensed matter physics, such as Weyl [3–19] and Dirac fermions [19–25] that were originally predicted in high-energy physics and recently observed in solid-state materials [26]. In topological semimetals, Weyl and Dirac points correspond to two- and four-fold degenerate linear band crossing points, hallmarks of relativistic particles with half-integer spins. Remarkably, the recent discovery of triply-degenerate points (TDPs) [27–39] in semimetals has opened an avenue for exploring new types of quasiparticles that have no analog in quantum field theory. Such TDPs possess effective integer spins while preserving Fermi statistics and linear dispersions.

Generally, the linearly dispersed quasiparticles near band degeneracies can be described by Hamiltonians with a spin-vector-momentum coupling  $\sim \mathbf{k} \cdot \mathbf{F}$ , where  $\mathbf{F} = (F_x, F_y, F_z)$  is a spin-vector. A degenerate point acts like a magnetic monopole in momentum space with a topological charge  $\mathcal{C}$  determined by the quantized Berry flux emanating from the point. In this context, a TDP with  $F = 1$  behaves like a three-component fermion with  $\mathcal{C} = \pm 2$ . However, it is well known that a full description of any large spin with  $F \geq 1$  naturally involves spin-tensors up to rank  $2F$ . For instance, there exist six rank-2 spin quadrupole tensors  $N_{ij} = (F_i F_j + F_j F_i)/2 - \delta_{ij} \mathbf{F}^2/3$  for  $F = 1$  in addition to the three vector components  $F_i$  ( $i = x, y, z$ ). Therefore two questions naturally arise. Can spin-tensor-momentum couplings produce novel types of TDPs with distinct topological properties? If so, how can such novel TDPs and associated spin-momentum couplings be realized in realistic systems?

In this paper, we address these two important questions by showing that two novel types of TDPs can emerge from the interplay between spin-vector- and spin-tensor-momentum couplings, and cold-atom optical lattices provide an attractive platform for their realizations. We call the TDPs described by the spin-vector-momentum coupling type-I [27–39] and the TDPs induced by spin-tensor-momentum couplings types II and III. Here are our main results. First, the three types have

different topological charges:  $\mathcal{C} = \pm 2, \pm 1$ , and 0 for types I, II, and III, respectively. A Zeeman field can lift them into Weyl points with distinct numbers and charges.

Second, the topological transitions between different types, accompanied by level crossings along high-symmetry lines, can be achieved by tuning the relative strengths of spin-vector- and spin-tensor-momentum couplings. By constructing a minimum three-band lattice model, we display different types of TDPs in the bulk and their exotic Fermi arcs at the surface.

Thirdly, since the type-II and type-III TDPs have not been discovered before, we propose the first experimental scheme for realizing type-II and required spin-momentum couplings using cold atoms in an optical lattice. Spin-vector-momentum coupling is crucial for many important condensed matter phenomena, and its recent experimental realization in ultracold atomic gases [40–51] has provided a highly controllable and disorder-free platform for exploring topological quantum matter. In cold atoms, spins are modeled by atomic hyperfine states, and a spin with  $F \geq 1$  can be naturally obtained. Nowadays, various types of spin-vector-momentum coupling for both spin-1/2 and spin-1 have been proposed and realized [40–54]. A scheme for realizing spin-tensor-momentum coupling of spin-1 atoms has also been proposed recently [55] with ongoing experimental efforts [56]. Our scheme is built on these experimentally available setups [50, 53] and may even pave the way for identifying solid-state materials with our novel types of TDPs.

*Triply-degenerate points.*—As a direct extension of a two-fold degenerate Weyl point described by  $H = \mathbf{k} \cdot \boldsymbol{\sigma}$ , the simplest TDP should be described by  $H = \mathbf{k} \cdot \mathbf{F}$  with the spin-1 vector  $\mathbf{F}$  [27–39]. The band structure around such a TDP is shown in Fig. 1(a), with a flat band located at the center and linear dispersions along all directions for the three bands. We label the band indices  $n$  for the lower, middle, and upper bands as  $-1, 0$ , and  $1$ , respectively. The corresponding wave function for band  $n$  is denoted as  $|\psi_n(\mathbf{k})\rangle$ . The topological property of the

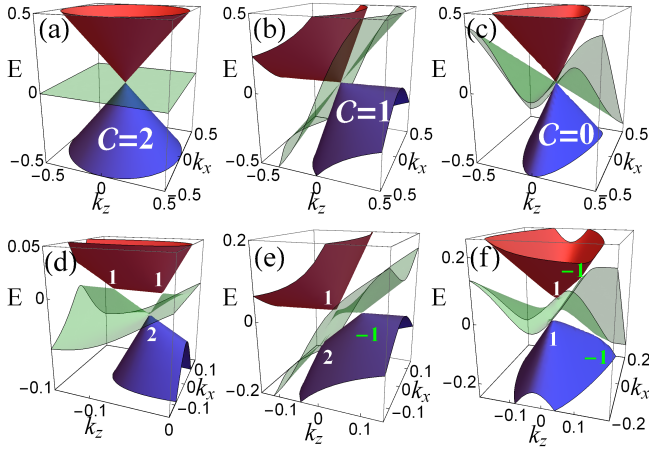


FIG. 1: (a)-(c) Band structures of three types of TDPs in the  $k_y = 0$  plane for model (2). (a) The type-I with  $\alpha = 1$  and  $\beta = 0$ . (b) The type-II with  $\alpha = 1$ ,  $\beta = 2$ , and  $N_{ij}$  is chosen as  $F_z^2$ . (c) The type-III with  $\alpha = 1$ ,  $\beta = 3$ , and  $N_{ij} = N_{xz}$ . (d)-(f) Splittings of three types of TDPs due to a Zeeman perturbation  $\varepsilon F_z$  with  $\varepsilon = 0.05$ . (d) The type-I splits into two linear Weyl points with  $C = 1$  and one double-Weyl point [65] with  $C = 2$ ; note that  $\beta = 0.5$  instead of 0 is used. (e) The type-II splits into two linear Weyl points with  $C = \pm 1$  and one double-Weyl point [65] with  $C = 2$ . (f) The type-III splits into four linear Weyl points with  $C = \pm 1$ .

TDP can be characterized by the first Chern numbers

$$C_n = \frac{1}{2\pi} \oint_{\mathcal{S}} \Omega_n(\mathbf{k}) \cdot d\mathbf{S}, \quad (1)$$

where  $\mathcal{S}$  is a closed surface enclosing the TDP and  $\Omega_n(\mathbf{k}) = \nabla_{\mathbf{k}} \times \langle \psi_n(\mathbf{k}) | i \nabla_{\mathbf{k}} | \psi_n(\mathbf{k}) \rangle$  is the Berry curvature of band  $n$ . For  $H = \mathbf{k} \cdot \mathbf{F}$ ,  $\Omega_n(\mathbf{k}) = -n\mathbf{k}/k^3$ , yielding  $C_n = -2n$  for the three bands. The monopole charge  $\mathcal{C}$  can be defined as the Chern number of the lower band, i.e.,  $\mathcal{C} = C_{-1}$ . Thus, this simplest TDP has  $\mathcal{C} = 2$  and behaves as a momentum-space monopole carrying two monopole charges.

Novel types of TDPs can emerge when spin-tensors are also considered. Since a constant spin-tensor perturbation  $\sim N_{ij}$  would break the three-fold degeneracy of  $H = \mathbf{k} \cdot \mathbf{F}$ , the stabilization of novel TDPs with linear dispersions requires the coupling of spin-tensors with momentum. For general linear Hamiltonians with  $H(\mathbf{k}) = -H(-\mathbf{k})$ , the property  $\Omega_n(\mathbf{k}) = \Omega_{-n}(-\mathbf{k})$  dictates  $C_{+1} = -C_{-1}$  for the upper and lower bands and  $C_0 = 0$  for the middle one. Moreover, it can be proved that  $|C_n| \leq 2$  for such linear Hamiltonians [57]. Therefore the monopole charges for TDPs can only be  $\pm 2$ ,  $\pm 1$ , and 0, indicating all possible TDPs can be classified into three types: type-I with  $\mathcal{C} = \pm 2$ , type-II with  $\mathcal{C} = \pm 1$ , and type-III with  $\mathcal{C} = 0$ .

All three types of TDPs can be illustrated using the following simple model [57]:

$$H(\mathbf{k}) = k_x F_x + k_y F_y + k_z (\alpha F_z + \beta N_{ij}), \quad (2)$$

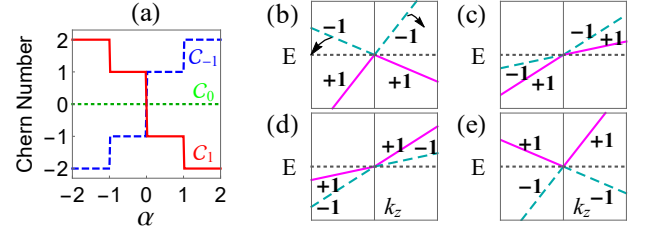


FIG. 2: Phase transitions between type-I and type-II TDPs by tuning  $\alpha$  while fixing  $\beta = 1$  in Eq. (2). (a) Chern numbers as functions of  $\alpha$  for the lower (dashed blue), middle (dotted green), and upper (solid red) bands. (b)-(e) Band structures along the  $k_x = k_y = 0$  line with  $\alpha = 2, 0.5, -0.5$ , and  $-2$ , respectively. We have labeled the Chern contributions of each branch:  $+1$  (solid magenta),  $-1$  (dashed cyan), and  $0$  (dotted black).

where the spin-tensor  $N_{ij}$  is coupled to  $k_z$ . By choosing different types of spin-tensors and tuning the relative strength of spin-tensor-momentum coupling  $\beta/\alpha$ , we find that (i) the three spin-tensors  $N_{xx}$ ,  $N_{yy}$ , and  $N_{xy}$  do not change the monopole charge  $\mathcal{C} = \pm 2$  of the type-I TDP, (ii) the tensor  $N_{zz}$  induces a  $\mathcal{C} = \pm 1$  TDP for  $|\beta| > |\alpha| \neq 0$ , dubbed type-II and depicted in Fig. 1(b), and (iii) the tensor  $N_{xz}$  or  $N_{yz}$  induces a  $\mathcal{C} = 0$  TDP for  $|\beta| > 2|\alpha| \neq 0$ , dubbed type-III and depicted in Fig. 1(c). Markedly, the energy dispersions are linear around all three types of TDPs.

**Type-II TDPs.**—Type-II TDPs can be induced from the type-I by choosing  $N_{ij}$  as  $F_z^2 = N_{zz} + \frac{2}{3}$  in Eq. (2). Since the additional spin-independent term  $2\beta k_z/3$  does not affect the eigenstates or any topological transition, we use  $F_z^2$  instead of  $N_{zz}$  for better presentation of our results. To study the transition between type-I and type-II TDPs due to the competition between spin-vector- and spin-tensor-momentum couplings, we fix  $\beta = 1$ , vary  $\alpha$ , and calculate  $C_n$  numerically using Eq. (1). As exhibited in Fig. 2(a), the lower-band Chern number  $C_{-1}$  (the monopole charge) changes from 2 (type-I) to  $\pm 1$  (type-II), and then to  $-2$  (type-I) with decreasing  $\alpha$ .

The topological transitions can be understood by the band crossings [57] along the  $k_x = k_y = 0$  line, as sketched in Figs. 2(b)-2(e). Note that the Chern number of each band has two contributions from the  $k_z < 0$  and  $k_z > 0$  branches in the surface integral of Eq. (1):  $\mathcal{C} = C_{k_z < 0} + C_{k_z > 0}$ . When  $\alpha > 1$ , the spin-vector-momentum coupling  $k_z F_z$  dominates and the model (2) is adiabatically connected to  $H = \mathbf{k} \cdot \mathbf{F}$  (type-I with  $\mathcal{C} = 2$ ); the contributions from the two branches of the lower band are  $C_{k_z < 0} = C_{k_z > 0} = +1$ , as shown in Fig. 2(b). With decreasing  $\alpha$ , the  $k_z < 0$  ( $k_z > 0$ ) branch of the lower band rotates clockwise (counterclockwise) in the  $E-k_z$  plane. At  $\alpha = 1$ , the middle band crosses simultaneously with the  $k_z < 0$  branch of the upper band and  $k_z > 0$  branch of the lower band. After the band crossing, as shown in Fig. 2(c), the lower band consists of two branches with

Chern contributions  $\mathcal{C}_{k_z < 0} = 1$  and  $\mathcal{C}_{k_z > 0} = 0$ , yielding a type-II TDP with  $\mathcal{C} = 1$ , in consistent with numerical results. With further decreasing  $\alpha$ , another level crossing occurs between the middle band and the  $k_z < 0$  ( $k_z > 0$ ) branch of lower (upper) band at  $\alpha = 0$ , as shown in Fig. 2(d). This crossing changes  $\mathcal{C}$  from 1 to  $-1$  and the resulting TDP is still type-II. A third band crossing occurs at  $\alpha = -1$ . For  $\alpha < -1$ , all bands are totally reversed compared to the  $\alpha > 1$  case as shown in Fig. 2(e), and the TDP is of type-I with  $\mathcal{C} = -2$ .

Type-I and type-II TDPs can be broken into different two-fold degenerate Weyl points in the presence of perturbations. With an additional Zeeman term  $\varepsilon F_z$  ( $\varepsilon \ll 1$ ) to Eq. (2), the eigenspectrum of the total Hamiltonian shows that both types of TDPs are broken into three nodal points located at  $W_{\pm} = (0, 0, -\varepsilon/(\alpha \pm \beta))$  and  $W_3 = (0, 0, -\varepsilon/\alpha)$  [57], as illustrated in Figs. 1(d)-1(e). The first two at  $W_{\pm}$  are linear Weyl points, which have the same charge  $\mathcal{C} = 1$  for type-I ( $|\beta| < |\alpha|$ ) but opposite charges  $\mathcal{C} = \pm 1$  for type-II ( $|\beta| > |\alpha|$ ) [57]. The third node at  $W_3$  is a multi-Weyl point [65] with  $\mathcal{C} = 2$ , whose dispersion is linear in the  $k_z$  direction but quadratic along the other two directions due to the indirect couplings between the lower and upper bands by  $F_x$  and  $F_y$ .

Splittings of TDPs can be understood using Fig. 2 with the small Zeeman field effectively lifting the middle band. For type-I in Fig. 2(b), the horizontal band would cross the two branches with the same Chern contributions, resulting in two linear Weyl points of the same monopole charge. Apart from the two linear Weyl points, there still exists a two-fold degenerate point with  $\mathcal{C} = 2$ . By contrast, type-II in Fig. 2(c) has a different configuration of energy levels, and the horizontal band would cross the two branches with opposite Chern contributions, leading to two linear Weyl points carrying opposite charges.

*Surface Fermi arcs.*—For a 3D Weyl semimetal, it is well known that a Fermi arc exists in the 2D surface Brillouin zone connecting two projected Weyl points of opposite charges [5]. In the above discussions, we have seen that there exist TDPs of opposite charges for both type-I and type-II. Therefore, it is important to examine and compare their surface consequences. The coexistence of TDPs with opposite charges can be best illustrated by the following minimal model on a cubic lattice:

$$H(\mathbf{k}) = F_x \sin k_x + F_y \sin k_y + t_0(F_z + \beta F_z^2) \\ (\cos k_x + \cos k_y + \cos k_z - 2 + \gamma), \quad (3)$$

which hosts two TDPs at  $\mathbf{k} = (0, 0, \pm \arccos(-\gamma))$  for  $|\gamma| < 1$ . As displayed in Figs. 3(a)-3(b), the band structure of model (3) with  $\gamma = -0.5$  features two TDPs at  $(0, 0, \pm\pi/3)$ . Around the two TDPs, the Hamiltonians can be expanded as  $H_{\pm}(\delta\mathbf{k}) = \delta k_x F_x + \delta k_y F_y \mp \frac{\sqrt{3}t_0}{2} \delta k_z (F_z + \beta F_z^2)$  to the linear order. The above effective Hamiltonian has the standard form of model (2), and the higher-order corrections would not affect the topolog-

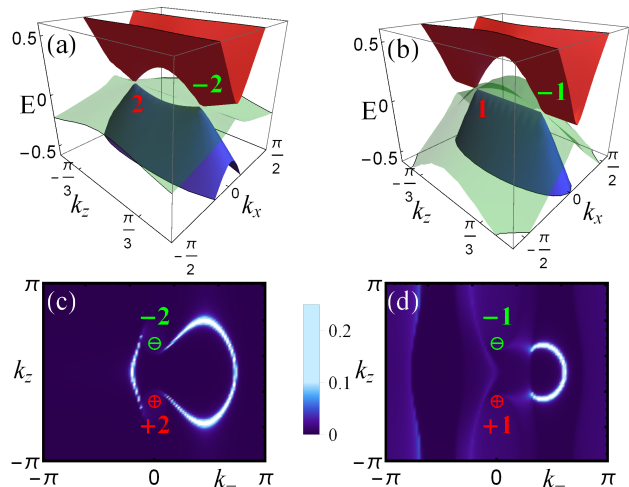


FIG. 3: Bulk band structures with TDPs and (110) surface spectral densities with Fermi arcs of model (3). (a) and (c) the type-I with  $\mathcal{C} = \pm 2$  and two surface arcs. (b) and (d) the type-II with  $\mathcal{C} = \pm 1$  and only one surface arc. In both cases, two TDPs appear at  $(0, 0, \pm\pi/3)$ , and each projected node is marked by its monopole charge. In our calculation,  $\gamma = -0.5$ ,  $\omega = 0.25$ , and  $t_0 = 0.5$  are used;  $\beta = 0.5$  is used in (a) and (c) while  $\beta = 1.5$  in (b) and (d).

ical properties. Therefore, the two TDPs belong to type-I for  $|\beta| < 1$  and type-II for  $|\beta| > 1$ .

To reveal and compare the surface hallmarks of the two types of TDPs, we impose a semi-infinite geometry with a (110) surface in our calculation. The surface Brillouin zone is expanded by  $(k_-, k_z)$  with  $k_- = (k_x - k_y)/\sqrt{2}$ . Since the middle band occupies most of the surface Brillouin zone at zero energy, we calculate the surface spectral density  $A(\omega, \mathbf{k}) = \text{Im}G(i\omega, \mathbf{k})/\pi$  [27] at a finite  $\omega$  in order to distinguish the surface and bulk states. Here  $G = (i\omega - H)^{-1}$  is the single-particle Green's function. For type-I, there is a pair of Fermi arcs, and each emanates from one projected TDP and ends at the other, as illustrated in Fig. 3(c). This clearly demonstrates the double monopole charges of type-I TDPs. For type-II, the two projected TDPs are connected by only one Fermi arc, as depicted in Fig. 3(d). This agrees well with the single monopole charges of type-II TDPs.

*Type-III TDPs.*—Spin-tensor  $N_{xz}$  or  $N_{yz}$  in model (2) can induce the topological transition of a TDP from type-I to type-III. Here we use  $N_{ij} = N_{xz}$  and  $\alpha = 1$  to illustrate the transition [57]. The TDP is of type-I for  $|\beta| < 2$  and type-III for  $|\beta| > 2$ . At  $|\beta| = 2$ , the bands cross along two lines  $k_z \pm k_x = k_y = 0$ , as shown in Fig. 4(b). At one of these two line nodes, e.g.,  $k_z - k_x = k_y = 0$ , the band energies are found to be  $-\beta k_z/2$  and  $(\beta \pm \sqrt{32 + \beta^2})k_z/4$ . Clearly, at  $\beta = 2$  the upper (lower) and middle bands cross at the  $k_z < 0$  ( $k_z > 0$ ) branch. The band crossing of the other line node is rather similar. Because each band crossing changes the Chern number

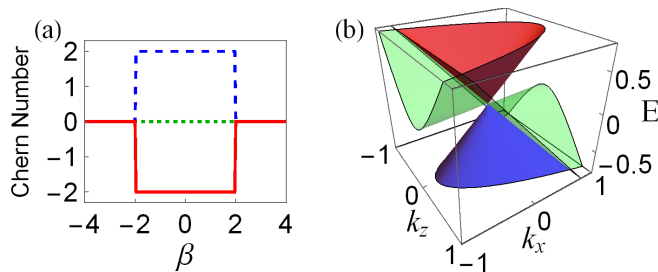


FIG. 4: Phase transitions between type-I and type-III TDPs by tuning  $\beta$  while fixing  $\alpha = 1$  in Eq. (2). (a) Chern numbers as functions of  $\beta$  for the lower (dashed blue), middle (dotted green), and upper (solid red) bands. (b) Band crossing at the two transition lines with  $\beta = 2$ .

by 1, and the crossings along the two lines are in the same branch, the Chern number must be changed by 2 as shown in Fig. 4(a), yielding a transition of the TDP from type-I with  $\mathcal{C} = \pm 2$  to type-III with  $\mathcal{C} = 0$ .

Although a type-III TDP has vanishing Chern numbers, it can exhibit non-trivial topological properties after breaking into linear Weyl points [57] in the presence of a small Zeeman field, as depicted in Fig. 1(f). There exist four Weyl points with  $\mathcal{C} = \pm 1$  located at  $(k_x, k_z) = (\pm\beta\varepsilon/(\beta - 2\alpha), 2\varepsilon/(\beta - 2\alpha))$  and  $(\pm\beta\varepsilon/(\beta + 2\alpha), -2\varepsilon/(\beta + 2\alpha))$  in the  $k_y = 0$  plane. From the above discussions, we can see that the three types of TDPs have different patterns of Weyl points after splitting, which results in distinct surface states since the surface Fermi arcs can only connect two Weyl points of opposite charges. Therefore, while for type-I the Fermi arcs only connect Weyl points originating from different TDPs, for type-II and type-III there may exist Fermi arcs connecting the Weyl points originating from the same TDP. These features may be used to identify TDPs of different types.

**Experimental realization and observation.**—The type-II TDPs can be realized by coupling three atomic hyperfine states (e.g., the  $6^2S_{1/2}$  ground-state manifold of  $^{133}\text{Cs}$  atom:  $g_1 = |4, -4\rangle$ ,  $g_0 = |3, -3\rangle$ , and  $g_{-1} = |4, -2\rangle$ ) using Raman beams in a spin-dependent square lattice [57]. The three states are used for mimicking the spin-1 degree of freedom, and the proposed scheme is based on techniques used in the recent experimental realization of 2D Rashba spin-orbit coupling for spin-1/2 in optical lattices [50]. The atom-light interactions include two crucial parts. One part is used for generating a spin-dependent square lattice potentials  $V_{g_{\pm 1}} \propto [\sin(2k_0x) + \sin(2k_0y)]$  and  $V_{g_0} \propto [-\sin(2k_0x) - \sin(2k_0y)]$  in the  $x$ - $y$  plane by one laser beam [53]. In the tight-binding limit, the  $g_{+1}$  and  $g_{-1}$  components stay on the same lattice sites. The other part is used for inducing the required spin-momentum couplings between the three hyperfine states, which can be achieved by adding another three Raman beams  $\mathbf{E}_{R_1, R_3} = E_{R_1, R_3} e^{\mp ik_m z} [\hat{x} \cos(2k_0y) \mp \hat{y} \cos(2k_0x)]$  and  $\mathbf{E}_{R_2} = E_{R_2} e^{ik_1 z} (i\hat{x} + \hat{y})$ . The result-

ing Raman couplings between  $g_{\pm 1}$  and  $g_0$  are  $M_{\pm 1, 0} \propto e^{i(k_1 \pm k_m)z} [\cos(2k_0x) \pm i \cos(2k_0y)]$  [50, 57]. Because the spatially dependent phase factors contain both spin-vector and spin-tensor components, they would produce both spin-vector- and spin-tensor-momentum couplings  $\sim k_z(k_1 F_z^2 + k_m F_z)$  in a chosen gauge. A careful analysis of the tight-binding model on the square lattice shows that the band structure contains two TDPs located at  $(0, 0)$  and  $(\pi, 0)$  in the  $k_x$ - $k_y$  plane at a constant  $k_z$ , similar to the case of model (3). Around these TDPs, the effective Hamiltonians have the standard form of Eq. (2), with the emergence of spin-tensor-momentum coupling. Type-II TDPs require  $|k_1| > |k_m|$ , which is naturally realized here since  $k_1 \approx \sqrt{k_m^2 + 4k_0^2}$  in our scheme [57].

The linear band dispersions and the three-fold degeneracy of a TDP may be detected experimentally using the momentum-resolved radio-frequency spectroscopy [66], as demonstrated in recent experiments for 2D spin-orbit coupled atomic gases through spin-injection methods [45–48]. Moreover, when the atomic gas is confined in a hard wall box potential similar to those realized in recent experiments [67, 68], surface Fermi arcs would emerge at the boundary, which may also be observed using the momentum-resolved radio-frequency spectroscopy.

**Discussions.**—We have proposed and demonstrated that the interplay between spin-vector- and spin-tensor-momentum couplings can induce two novel types of TDPs possessing distinct topological properties (e.g., Chern numbers, breaking into Weyl points, surface Fermi arcs, etc.) from the already discovered type-I TDP in solid-state materials. In particular, our proposed spin-tensor-momentum coupling mechanism should open a broad avenue for exploring novel topological quantum matter, and our results have already showcased two prime examples, i.e., the type-II and type-III TDPs.

Our results may motivate further theoretical and experimental studies of TDPs and other novel topological matter. Although our proposed experimental scheme is for cold-atom optical lattices, similar type-II and type-III TDPs may also be found in some solid-state materials in certain space groups by first-principles calculations [69] and angle-resolved photoemission spectroscopy experiments. Moreover, we note that recently a type-I TDP has been experimentally realized in the parameter space of a superconducting qutrit [70], where the type-II and type-III TDPs may also be realized similarly. Finally, although we focus on the spin-1 rank-2 tensors for the purpose of studying TDPs, there exist higher-rank spin-tensors for higher spin systems, whose couplings with momentum may give rise to nontrivial topological matter with unprecedented properties.

This work is supported by NSF (PHY-1505496), ARO (W911NF-17-1-0128), AFOSR (FA9550-16-1-0387), and UTD Research Enhancement Funds.



- 
- \* Electronic address: [chuanwei.zhang@utdallas.edu](mailto:chuanwei.zhang@utdallas.edu)
- [1] M. Z. Hasan and C. L. Kane, *Colloquium: Topological insulators*, *Rev. Mod. Phys.* **82**, 3045 (2010).
  - [2] X.-L. Qi and S.-C. Zhang, *Topological insulators and superconductors*, *Rev. Mod. Phys.* **81**, 109 (2009).
  - [3] G. Volovik, *The Universe in a Helium Droplet* (Oxford University Press, Oxford, 2003).
  - [4] S. Murakami, *Phase transition between the quantum spin Hall and insulator phases in 3D: emergence of a topological gapless phase*, *New J. Phys.* **9**, 356 (2007).
  - [5] X. G. Wan, A. M. Turner, A. Vishwanath, and S. Y. Savrasov, *Topological semimetal and Fermi-arc surface states in the electronic structure of pyrochlore iridates*, *Phys. Rev. B* **83**, 205101 (2011).
  - [6] A. A. Burkov and L. Balents, *Weyl Semimetal in a topological insulator multilayer*, *Phys. Rev. Lett.* **107**, 127205 (2011).
  - [7] M. Hirschberger et al., *The chiral anomaly and thermopower of Weyl fermions in the half-Heusler GdPtBi*, *Nat. Mater.* **15**, 1161 (2016).
  - [8] S.-M. Huang et al., *A Weyl fermion semimetal with surface Fermi arcs in the transition metal monpnictide TaAs class*, *Nat. Commun.* **6**, 7373 (2015).
  - [9] B. Q. Lv et al., *Experimental discovery of Weyl semimetal TaAs*, *Phys. Rev. X* **5**, 031013 (2015).
  - [10] B. Q. Lv et al., *Observation of Weyl points in TaAs*, *Nat. Phys.* **11**, 724 (2015).
  - [11] C. Shekhar et al., *Observation of chiral magnetotransport in RPtBi topological Heusler compounds*, [arXiv:1604.01641](https://arxiv.org/abs/1604.01641).
  - [12] H. M. Weng, C. Fang, Z. Fang, B. A. Bernevig, and X. Dai, *Weyl semimetal phase in noncentrosymmetric transition-metal monophosphides*, *Phys. Rev. X* **5**, 011029 (2015).
  - [13] S.-Y. Xu et al., *Discovery of a Weyl fermion state with Fermi arcs in niobium arsenide*, *Nat. Phys.* **11**, 748 (2015).
  - [14] S.-Y. Xu et al., *Discovery of a Weyl fermion semimetal and topological Fermi arcs*, *Science* **349**, 613 (2015).
  - [15] L. X. Yang et al., *Weyl semimetal phase in the noncentrosymmetric compound TaAs*, *Nat. Phys.* **11**, 728 (2015).
  - [16] L. Lu et al., *Experimental observation of Weyl points*, *Science* **349**, 622 (2015).
  - [17] C.-C. Liu, J.-J. Zhou, Y. Yao, and F. Zhang, *Weak topological insulators and composite Weyl semimetals:  $\beta$ -Bi<sub>4</sub>X<sub>4</sub> (X=Br,I)*, *Phys. Rev. Lett.* **116**, 066801 (2016).
  - [18] A. Lau, K. Koepf, J. van den Brink, and C. Ortix, *Generic coexistence of Fermi arcs and Dirac cones on the surface of time-reversal invariant Weyl semimetals*, *Phys. Rev. Lett.* **119**, 076801 (2017).
  - [19] S. A. Yang, H. Pan, and F. Zhang, *Dirac and Weyl superconductors in three dimensions*, *Phys. Rev. Lett.* **113**, 046401 (2014).
  - [20] Z. K. Liu et al., *A stable three-dimensional topological Dirac semimetal Cd<sub>3</sub>As<sub>2</sub>*, *Nat. Mater.* **13**, 677 (2014).
  - [21] J. A. Steinberg et al., *Bulk Dirac points in distorted spinels*, *Phys. Rev. Lett.* **112**, 036403 (2014).
  - [22] Z. J. Wang et al., *Dirac semimetal and topological phase transitions in A<sub>3</sub>Bi (A=Na, K, Rb)*, *Phys. Rev. B* **85**, 195320 (2012).
  - [23] J. Xiong et al., *Evidence for the chiral anomaly in the Dirac semimetal Na<sub>3</sub>Bi*, *Science* **350**, 413 (2015).
  - [24] S. M. Young et al., *Dirac semimetal in three dimensions*, *Phys. Rev. Lett.* **108**, 140405 (2012).
  - [25] Z. K. Liu et al., *Discovery of a three-dimensional topological dirac semimetal, Na<sub>3</sub>Bi*, *Science* **343**, 864 (2014).
  - [26] A. A. Burkov, *Topological semimetals*, *Nat. Mater.* **15**, 1145 (2016).
  - [27] B. Bradlyn et al., *Beyond Dirac and Weyl fermions: Unconventional quasiparticles in conventional crystals*, *Science* **353**, 6299 (2016).
  - [28] B. Q. Lv et al., *Observation of three-component fermions in the topological semimetal molybdenum phosphide*, *Nature* **546**, 627 (2017).
  - [29] H. Yang et al., *Prediction of triple point fermions in simple half-Heusler topological insulators*, *Phys. Rev. Lett.* **119**, 136401 (2017).
  - [30] G. W. Winkler, Q.-S. Wu, M. Troyer, P. Krogstrup, and A. A. Soluyanov, *Topological phases in InAs<sub>1-x</sub>Sb<sub>x</sub>: From novel topological semimetal to Majorana wire*, *Phys. Rev. Lett.* **117**, 076403 (2016).
  - [31] H. M. Weng, C. Fang, Z. Fang, and X. Dai, *Topological semimetals with triply degenerate nodal points in  $\theta$ -phase tantalum nitride*, *Phys. Rev. B* **93**, 241202(R) (2016).
  - [32] Z. M. Zhu, G. W. Winkler, Q. S. Wu, J. Li, and A. A. Soluyanov, *Triple point topological metals*, *Phys. Rev. X* **6**, 031003 (2016).
  - [33] H. M. Weng, C. Fang, Z. Fang, and X. Dai, *Coexistence of Weyl fermion and massless triply degenerate nodal points*, *Phys. Rev. B* **94**, 165201 (2016).
  - [34] G. Q. Chang et al., *Nexus fermions in topological symmorphic crystalline metals*, *Sci. Rep.* **7**, 1688 (2017).
  - [35] I. C. Fulga and A. Stern, *Triple point fermions in a minimal symmorphic model*, *Phys. Rev. B* **95**, 241116(R) (2017).
  - [36] G. Q. Chang et al., *Unconventional chiral fermions and large topological fermi arcs in RhSi*, *Phys. Rev. Lett.* **119**, 206401 (2017).
  - [37] C. Y. Zhong et al., *Three-dimensional pentagon carbon with a genesis of emergent fermions*, *Nat. Commun.* **8**, 15641 (2017).
  - [38] J. B. Yu, B. H. Yan, and C.-X. Liu, *Model Hamiltonian and time reversal breaking topological phases of antiferromagnetic half-Heusler materials*, *Phys. Rev. B* **95**, 235158 (2017).
  - [39] X. M. Zhang, Z.-M. Yu, X.-L. Sheng, H. Y. Yang, and S. A. Yang, *Coexistence of four-band nodal rings and triply degenerate nodal points in centrosymmetric metal diborides*, *Phys. Rev. B* **95**, 235116 (2017).
  - [40] Y.-J. Lin, K. Jiménez-García, and I. B. Spielman, *Spin-orbit-coupled Bose-Einstein condensates*, *Nature* **471**, 83 (2011).
  - [41] Z. K. Fu, P. J. Wang, S. J. Chai, L. H. Huang, and J. Zhang, *Bose-Einstein condensate in a light-induced vector gauge potential using 1064-nm optical-dipole-trap lasers*, *Phys. Rev. A* **84**, 043609 (2011).
  - [42] J.-Y. Zhang et al., *Collective dipole oscillations of a spin-orbit coupled Bose-Einstein condensate*, *Phys. Rev. Lett.* **109**, 115301 (2012).
  - [43] C. Qu, C. Hamner, M. Gong, C. Zhang, and P. Engels, *Observation of Zitterbewegung in a spin-orbit coupled Bose-Einstein condensate*, *Phys. Rev. A* **88**, 021604(R) (2013).
  - [44] A. J. Olson et al., *Tunable Landau-Zener transitions in a*

- spin-orbit-coupled Bose-Einstein condensate*, *Phys. Rev. A* **90**, 013616 (2014).
- [45] P. Wang et al., *Spin-orbit coupled degenerate Fermi gases*, *Phys. Rev. Lett.* **109**, 095301 (2012).
- [46] L. W. Cheuk et al., *Spin-injection spectroscopy of a spin-orbit coupled Fermi gas*, *Phys. Rev. Lett.* **109**, 095302 (2012).
- [47] L. H. Huang et al., *Experimental realization of two-dimensional synthetic spin-orbit coupling in ultracold Fermi gases*, *Nat. Phys.* **12**, 540 (2016).
- [48] Z. M. Meng et al., *Experimental observation of a topological band gap opening in ultracold Fermi gases with two-dimensional spin-orbit coupling*, *Phys. Rev. Lett.* **117**, 235304 (2016).
- [49] R. A. Williams, M. C. Beeler, L. J. LeBlanc, and I. B. Spielman, *Raman-induced interactions in a single-component Fermi gas near an s-Wave Feshbach resonance*, *Phys. Rev. Lett.* **111**, 095301 (2013).
- [50] Z. Wu et al., *Realization of two-dimensional spin-orbit coupling for Bose-Einstein condensates*, *Science* **354**, 83 (2016).
- [51] D. Campbell et al., *Magnetic phases of spin-1 spin-orbit-coupled Bose gases*, *Nat. Commun.* **7**, 10897 (2016).
- [52] B. M. Anderson, G. Juzeliūnas, V. M. Galitski, and I. B. Spielman, *Synthetic 3D spin-orbit coupling*, *Phys. Rev. Lett.* **108**, 235301 (2012).
- [53] B.-Z. Wang et al., *Dirac-, Rashba-, and Weyl-type spin-orbit couplings: Toward experimental realization in ultracold atoms*, *Phys. Rev. A* **97**, 011605(R).
- [54] Y. Li, X. Zhou, C. Wu, *Three-dimensional quaternionic condensations, Hopf invariants, and skyrmion lattices with synthetic spin-orbit coupling*, *Phys. Rev. A* **93**, 033628 (2016).
- [55] X.-W. Luo, K. Sun, and C. Zhang, *Spin-tensor-momentum-coupled Bose-Einstein condensates*, *Phys. Rev. Lett.* **119**, 193001 (2017).
- [56] Private communications with P. Engels and J. Zhang.
- [57] See “Supplementary Materials” for more discussions on topological invariants, another model exhibiting TDPs, phase transitions, the splitting of TDPs and our experimental scheme, which includes Refs. [58–64].
- [58] E. Majorana, *Atomi orientati in campo magnetico variabile*, *Nuovo Cimento* **9**, 43 (1932).
- [59] J. Schwinger, *Quantum Theory of Angular Momentum*, edited by L. C. Biendeharn and H. Van Dam (Academic Press, New York, 1965).
- [60] J. H. Hannay, *The Berry phase for spin in the Majorana representation*, *J. Phys. A* **31**, L53 (1998).
- [61] P. Bruno, *Quantum geometric phase in Majorana stellar representation: Mapping onto a many-body Aharonov-Bohm phase*, *Phys. Rev. Lett.* **108**, 240402 (2012); Q. Niu, *Viewpoint: A quantum constellation*, *Physics* **5**, 65 (2012).
- [62] H. D. Liu and L. B. Fu, *Representation of Berry phase by the trajectories of Majorana stars*, *Phys. Rev. Lett.* **113**, 240403 (2014).
- [63] R. Barnett, D. Podolsky, and G. Refael, *Geometrical approach to hydrodynamics and low-energy excitations of spinor condensates*, *Phys. Rev. B* **80**, 024420 (2009).
- [64] B. Andrei Bernevig and Taylor L. Hughes, *Topological Insulators and Topological Superconductors*.
- [65] C. Fang, M. J. Gilbert, X. Dai, and B. A. Bernevig, *Multi-Weyl topological semimetals stabilized by point group symmetry*, *Phys. Rev. Lett.* **108**, 266802 (2012).
- [66] J. T. Stewart, J. P. Gaebler, and D. S. Jin, *Using photoemission spectroscopy to probe a strongly interacting Fermi gas*, *Nature* **454**, 744 (2008).
- [67] A. L. Gaunt, T. F. Schmidutz, I. Gotlibovych, R. P. Smith, and Z. Hadzibabic, *Bose-Einstein condensation of atoms in a uniform potential*, *Phys. Rev. Lett.* **110**, 200406 (2013).
- [68] B. Mukherjee, Z. Yan, P. B. Patel, Z. Hadzibabic, T. Yefsah, J. Struck, and M. W. Zwierlein, *Homogeneous atomic Fermi gases*, *Phys. Rev. Lett.* **118**, 123401 (2017).
- [69] Private communications with H. M. Weng and B. Wieder.
- [70] X. Tan, D.-W. Zhang, Q. Liu, G. Xue, H.-F. Yu, Y.-Q. Zhu, H. Yan, S.-L. Zhu, Y. Yu, *Topological Maxwell metal bands in a superconducting qutrit*, *Phys. Rev. Lett.* **120**, 130503 (2018).

## Supplementary Materials

### Proof of $|\mathcal{C}| \leq 2$ for TDPs of Linear Hamiltonians

In this section, we unveil the geometric meaning of the topological invariant defined in Eq. (1) of the main text and give an intuitive yet rigorous proof for  $|\mathcal{C}| \leq 2$  in a more general setting. To this end, we introduce a powerful tool—Majorana stellar representation [58], which maps quantum states in a high-dimensional Hilbert space onto several points (i.e., Majorana stars) on the Bloch sphere—the state space of a quantum spin-1/2 system. In this representation, any spin-1 state can be mapped to two Majorana stars on the Bloch sphere. For convenience, the integral surface  $\mathcal{S}$  in Eq. (1) is chosen as the unit sphere.

We start with the well-known spin-1/2 system. In a chosen basis (denoted as  $|\uparrow\rangle, |\downarrow\rangle$ ), an arbitrary state can be written as  $|u\rangle = \cos\frac{\theta}{2}|\uparrow\rangle + e^{i\phi}\sin\frac{\theta}{2}|\downarrow\rangle$  ( $0 \leq \theta \leq \pi, 0 \leq \phi < 2\pi$ ). The state  $|u\rangle$  is represented by a point  $\mathbf{u} = (\sin\theta \cos\phi, \sin\theta \sin\phi, \cos\theta)$  on the Bloch sphere, with  $\theta$  and  $\phi$  denoting the colatitude and longitude in the spherical coordinate. For a Weyl point  $H(\mathbf{k}) = -\mathbf{k} \cdot \boldsymbol{\sigma}$ ,  $|u\rangle$  is the lower state at  $\hat{\mathbf{k}} = (\sin\theta \cos\phi, \sin\theta \sin\phi, \cos\theta)$ , that is, the Majorana star  $\mathbf{u}$  on the Bloch sphere coincides with  $\hat{\mathbf{k}}$  on the integral surface  $\mathcal{S}$ . The Chern number (monopole charge) of the Weyl point is then

$$\mathcal{C} = \frac{1}{2\pi} \oint_{\mathcal{S}} \boldsymbol{\Omega}(\mathbf{k}) \cdot d\mathbf{S} = -\frac{1}{4\pi} \oint_{\mathcal{S}} d\theta d\phi \mathbf{u} \cdot \partial_{\theta} \mathbf{u} \times \partial_{\phi} \mathbf{u} = -1. \quad (4)$$

Clearly,  $\mathcal{C}$  counts how many times the Majorana star covers the Bloch sphere by varying  $\hat{\mathbf{k}}$  on  $\mathcal{S}$ .

For a spin-1 system, any quantum state can be formulated as  $|\psi\rangle = f_{-1}|1, -1\rangle + f_0|1, 0\rangle + f_1|1, 1\rangle$  in a given basis  $|1, m\rangle$  ( $m = \pm 1, 0$ ). The basis state can be rewritten using the creation and annihilation operators  $a^{\dagger}, a$ , and  $b^{\dagger}, b$  of Schwinger bosons [59]:  $|1, m\rangle = \frac{(a^{\dagger})^{1+m}(b^{\dagger})^{1-m}}{(1+m)!(1-m)!}|\emptyset\rangle$  ( $|\emptyset\rangle$  is a vacuum state). The Schwinger bosons satisfy the standard bosonic commutation relations:  $[a, a^{\dagger}] = [b, b^{\dagger}] = 1$  and all others are zero. The spin-1 operators are represented by two types of Schwinger bosons as:

$$F^{+} = F_x + iF_y = a^{\dagger}b, \quad F^{-} = F_x - iF_y = b^{\dagger}a, \quad F_z = \frac{1}{2}(a^{\dagger}a - b^{\dagger}b), \quad (5)$$

along with the constraint  $n_a + n_b \equiv a^{\dagger}a + b^{\dagger}b = 2F$ . Here  $n_a$  and  $n_b$  are the occupation numbers of Schwinger bosons. The spin-1 basis state  $|1, m\rangle$  is then equivalent to the state  $|n_a, n_b\rangle = |1+m, 1-m\rangle$ . It is easy to verify the commutation relations for spin operators:  $[F_i, F_j] = i\epsilon_{ijk}F_k$ . Now the spin-1 state  $|\psi\rangle$  can be factorized as [58–63]

$$|\psi\rangle = \frac{1}{N_1} \prod_{j=1}^2 (\cos\frac{\theta_j}{2}a^{\dagger} + \sin\frac{\theta_j}{2}e^{i\phi_j}b^{\dagger})|\emptyset\rangle, \quad (6)$$

where  $N_1$  is the normalization factor, and the parameters  $\theta_j$  and  $\phi_j$  can be determined by  $\sum_{j=0}^2 \frac{(-1)^j f_{1-j}}{\sqrt{(2-j)!j!}} y^{2-j} = 0$  with  $y_j = \tan\frac{\theta_j}{2}e^{i\phi_j}$ . By denoting  $a^{\dagger}|\emptyset\rangle = |\uparrow\rangle$ ,  $b^{\dagger}|\emptyset\rangle = |\downarrow\rangle$ , it follows from Eq. (6) that  $|\psi\rangle$  is represented by the two Majorana stars located at  $\mathbf{u}_j = (\sin\theta_j \cos\phi_j, \sin\theta_j \sin\phi_j, \cos\theta_j)$  ( $j = 1, 2$ ) on the Bloch sphere. Within the Majorana stellar representation, now we are ready to prove  $|\mathcal{C}| \leq 2$  for a spin-1 TDP.

Because the Chern number is defined on a closed two-dimensional surface  $\mathcal{S}$  with no boundary, a nonzero Chern number indicates that we cannot choose a gauge that is continuous and single valued on the whole surface  $\mathcal{S}$  (which yields  $\mathcal{C} = 0$  by Stokes' theorem).  $\mathcal{S}$  is then separated into different regions as sketched in Fig. 5(a). Inside each region, we can choose a smooth gauge and use the Stokes' theorem:

$$\begin{aligned} 2\pi\mathcal{C} &= \oint_{\mathcal{S}} \boldsymbol{\Omega}(\mathbf{k}) \cdot d\mathbf{S} = \iint_{\mathcal{S}_a} \boldsymbol{\Omega}(\mathbf{k}) \cdot d\mathbf{S} + \iint_{\mathcal{S}_b} \boldsymbol{\Omega}(\mathbf{k}) \cdot d\mathbf{S} \\ &= \int_{\Gamma} \mathbf{A}^a \cdot d\mathbf{l} - \int_{\Gamma} \mathbf{A}^b \cdot d\mathbf{l} = \gamma^a - \gamma^b. \end{aligned} \quad (7)$$

Here  $\mathbf{A}^a$  and  $\mathbf{A}^b$  are the gauge potentials associated with Berry curvature  $\boldsymbol{\Omega}(\mathbf{k})$  in each region:  $\nabla \times \mathbf{A}^{a,b} = \boldsymbol{\Omega}(\mathbf{k})$ .  $\gamma^a$  and  $\gamma^b$  are the accumulated Berry phases along the path  $\Gamma$  (i.e., the boundary of  $\mathcal{S}_a$  and  $\mathcal{S}_b$ ) under different gauges. Although  $\mathbf{A}^{a,b}$  and  $\gamma^{a,b}$  are gauge-dependent,  $\boldsymbol{\Omega}(\mathbf{k})$  is not. From the Majorana stellar representation, the Berry phase

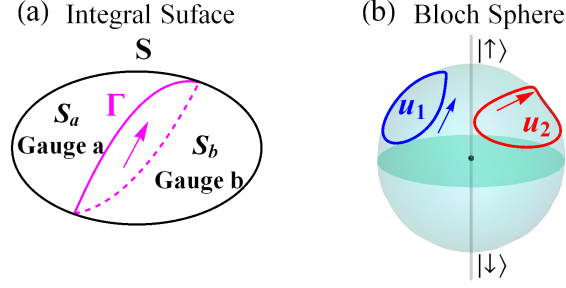


FIG. 5: (a) The integral surface  $\mathcal{S}$  in momentum space is split into two pieces. In each piece, we can choose a smooth gauge.  $\Gamma$  is the boundary between the two pieces. (b) A spin-1 state is represented by two Majorana stars  $\mathbf{u}_1$  and  $\mathbf{u}_2$  on the Bloch sphere. The Berry phase is determined by the trajectories of two Majorana stars.

for a spin-1 system in a chosen gauge can be elegantly formulated as [60–62]

$$\gamma = \gamma_S + \gamma_C \equiv - \sum_{j=1}^2 \frac{1}{2} \oint (1 - \cos \theta_j) d\phi_j - \frac{1}{2} \oint \frac{(d\mathbf{u}_1 - d\mathbf{u}_2) \cdot (\mathbf{u}_1 \wedge \mathbf{u}_2)}{3 + \mathbf{u}_1 \cdot \mathbf{u}_2}. \quad (8)$$

The first term  $\gamma_S = \sum_{j=1}^2 \int_{\Gamma} \langle u_j | i \nabla | u_j \rangle \cdot d\mathbf{l}$  describes the contributions from the solid angles subtended by the trajectories of two Majorana stars, as shown in Fig. 5(b). While the second term, which is gauge invariant [63], comes from their correlations. It is clear from Eq. (8) that a nonzero Chern number solely comes from the gauge mismatch of the two Majorana stars. Using Stokes' theorem,

$$\begin{aligned} \mathcal{C} &= \frac{1}{2\pi} (\gamma_S^a - \gamma_S^b) = -\frac{1}{2\pi} \sum_{j=1}^2 \text{Im} \left[ \iint_{S_a} \langle \nabla u_j^a | \times | \nabla u_j^a \rangle + \iint_{S_b} \langle \nabla u_j^b | \times | \nabla u_j^b \rangle \cdot d\mathcal{S} \right] \\ &= -\frac{1}{2\pi} \sum_{j=1}^2 \text{Im} \oint_{\mathcal{S}} (\langle \nabla u_j | \times | \nabla u_j \rangle) \cdot d\mathcal{S} = -\frac{1}{4\pi} \sum_{j=1}^2 \oint_{\mathcal{S}} d\theta d\phi \mathbf{u}_j \cdot \partial_{\theta} \mathbf{u}_j \times \partial_{\phi} \mathbf{u}_j. \end{aligned} \quad (9)$$

Geometrically,  $\mathcal{C}$  is the sum of the covering numbers of the two Majorana stars on the Bloch sphere. To prove  $|\mathcal{C}| \leq 2$ , we only need to show, each Majorana star covers Bloch sphere at most once for our system. In another words, given two Majorana stars  $\mathbf{u}_1$  and  $\mathbf{u}_2$  on the Bloch sphere, we can find at most one  $\hat{\mathbf{k}}$  on  $\mathcal{S}$ , with  $\mathbf{u}_1$  and  $\mathbf{u}_2$  being the projection of the lowest state of  $H(\hat{\mathbf{k}})$  in the Majorana stellar representation.

This is done by reductio ad absurdum. We can construct a unique spin-1 state  $|\psi\rangle$  (up to an irrelevant phase) using  $\mathbf{u}_1$  and  $\mathbf{u}_2$ . Suppose both  $\hat{\mathbf{k}}_1$  and  $\hat{\mathbf{k}}_2$  satisfy the condition:  $H(\hat{\mathbf{k}}_1)|\psi\rangle = e_1|\psi\rangle$  and  $H(\hat{\mathbf{k}}_2)|\psi\rangle = e_2|\psi\rangle$ , with  $e_1$  and  $e_2$  the lowest-state energies. Because our Hamiltonian is traceless, the sum of all the three eigenvalues must be 0. It follows that  $e_{1,2} < 0$  (which cannot be 0 due to the gapped spectrum on  $\mathcal{S}$ ). From  $\hat{\mathbf{k}}_1$  and  $\hat{\mathbf{k}}_2$ , we can find a point  $\hat{\mathbf{k}}^* = \frac{e_2 \hat{\mathbf{k}}_1 - e_1 \hat{\mathbf{k}}_2}{|e_2 \hat{\mathbf{k}}_1 - e_1 \hat{\mathbf{k}}_2|}$  on  $\mathcal{S}$ . The linearity of Hamiltonian yields  $H(\hat{\mathbf{k}}^*)|\psi\rangle = \frac{1}{|e_2 \hat{\mathbf{k}}_1 - e_1 \hat{\mathbf{k}}_2|} [e_2 H(\hat{\mathbf{k}}_1)|\psi\rangle - e_1 H(\hat{\mathbf{k}}_2)|\psi\rangle] = 0$ , in contradiction to the traceless nature of the Hamiltonian. Therefore, there is at most one  $\hat{\mathbf{k}}$  on  $\mathcal{S}$  for any two given Majorana stars  $\mathbf{u}_1$  and  $\mathbf{u}_2$  on the Bloch sphere. This concludes that  $|\mathcal{C}| \leq 2$  in Eq. (9).

For a linear Hamiltonian with  $H(\mathbf{k}) = -H(-\mathbf{k})$ , we have  $C_{+1} = -C_{-1}$  for the upper and lower bands and  $C_0 = 0$  for the middle band.  $|\mathcal{C}_n| \leq 2$  determines that there are only three types of TDPs, classified by  $\mathcal{C} = \pm 2, \pm 1, 0$ , as discussed in the main text. We note that in the above proof, only the  $\mathbf{k}$ -linear and traceless properties of the Hamiltonians are used. Therefore, our classification of TDPs is quite general and can be used for all spin-vector and spin-tensor momentum coupling cases, given the fact that all the spin-vectors and spin-tensors are traceless. Finally, although we consider the traceless Hamiltonians in the above proof, any additional spin-independent linear term such as  $\eta k_z$  in the Hamiltonian only rotates the eigenspectrum in the momentum space without changing the eigenstates, and therefore all topological invariances and topological phase transitions do not change.



### An extended model for TDPs

Besides the simple model with one spin-tensor momentum coupling term in the main text, the above general classification of TDPs also applies to more complicated models with two spin-tensors coupled to momenta, that is,

$$H(\mathbf{k}) = \mathbf{k} \cdot \mathbf{F} + \gamma_1 k_y N_{ij} + \gamma_2 k_z N_{i'j'}. \quad (10)$$

The first term is the standard spin-vector-momentum coupling. Without loss of generality, the two spin-tensors  $N_{ij}$  and  $N_{i'j'}$  are respectively coupled to  $k_y$  and  $k_z$ .  $\gamma_1$  and  $\gamma_2$  are the coupling strengths. In Table I, we have listed all the possible new types of TDPs.

$N_{ij} \backslash N_{i'j'}$	$N_{xx}$	$N_{xy}$	$N_{yy}$	$N_{xz}$	$N_{yz}$	$N_{zz}$
$N_{xx}$	×	×	×	III	III	II
$N_{xy}$	III	III	III	III	III	II,III
$N_{yy}$	II	II	II	II,III	II,III	II,III
$N_{xz}$	×	×	×	III	III	II
$N_{yz}$	III	III	III	III	II,III	II,III
$N_{zz}$	×	×	×	III	III	II

TABLE I: Type-II and type-III TDPs induced by two spin-tensor-momentum coupling terms via tuning their strengths  $\gamma_1$  and  $\gamma_2$ . “×” means the corresponding spin-tensor-momentum couplings cannot change the type of the original TDP at  $\gamma_1 = \gamma_2 = 0$ , which is always type-I.

It is clear from Table I that all induced TDPs still belong to the three types, classified by different Chern numbers:  $C = \pm 2, \pm 1, 0$ . The inclusion of more spin-tensor-momentum couplings can trigger more topological phase transitions, due to the level crossings induced by these terms. Similarly, we can discuss these level crossings, Zeeman splittings, etc. Moreover, we have checked all  $6 \times 6 \times 6 = 216$  cases with three spin-tensors coupled into the Hamiltonian. These results are in consistent with our classification and general discussions.

### Calculation of the topological invariant $\mathcal{C}$

For a given Hamiltonian  $H(\mathbf{k})$ , we can calculate its three eigenstates  $|\psi_n(\mathbf{k})\rangle$ , from which we can determine the Berry curvature  $\Omega_n(\mathbf{k})$ . The Chern number of each band is defined as  $\mathcal{C}_n = \frac{1}{2\pi} \oint_{\mathbf{S}} \Omega_n(\mathbf{k}) \cdot d\mathbf{S}$ , where the integral surface  $\mathbf{S}$  is chosen as a sphere of radius  $k$  around the TDP, and the surface element  $d\mathbf{S} = k^2 \sin \theta d\theta d\phi \frac{\mathbf{k}}{k}$ .

For the standard Hamiltonian  $\mathbf{k} \cdot \mathbf{F}$ , the eigenvalues are  $-k, 0, k$ ; by taking  $\mathbf{k} = k(\sin \theta \cos \phi, \sin \theta \sin \phi, \cos \theta)$ , the corresponding eigenstates are  $|-1\rangle = \left( \sin^2 \frac{\theta}{2} e^{-i\phi}, -\frac{\sin \theta}{\sqrt{2}}, \cos^2 \frac{\theta}{2} e^{i\phi} \right)^T$ ,  $|0\rangle = \left( -\frac{\sin \theta}{\sqrt{2}} e^{-i\phi}, \cos \theta, \frac{\sin \theta}{\sqrt{2}} e^{i\phi} \right)^T$ ,  $|1\rangle = \left( \cos^2 \frac{\theta}{2} e^{-i\phi}, \frac{\sin \theta}{\sqrt{2}}, \sin^2 \frac{\theta}{2} e^{i\phi} \right)^T$ . The resulting Berry curvature for each band is found to be  $\Omega_n(\mathbf{k}) = -n\mathbf{k}/k^3$ , yielding  $\mathcal{C}_n = \frac{1}{2\pi} \int_0^\pi \int_0^{2\pi} k^2 \sin \theta d\theta d\phi \int_0^{2\pi} d\phi \left( -n \frac{k}{k^3} \right) = -n \int_0^\pi \sin \theta d\theta = -2n$ . For comparison, the Berry curvature of a spin-1/2 is  $\Omega_n(\mathbf{k}) = -n \frac{\mathbf{k}}{2k^3}$  [64], which gives  $\mathcal{C}_n = -n$ . As  $n = \mp 1$ ,  $\mathcal{C}_n = \pm 1$ .

For a general Hamiltonian with spin-tensors, the eigenstates and Berry curvatures cannot be determined analytically, therefore all calculations are done numerically.

### Determination of phase transition points

The inclusion of spin-tensors  $N_{ij}$  can induce a series of topological phase transitions, accompanied by level-crossings in  $\mathbf{k}$  space. To determine these phase transition points and level-crossing lines analytically, we utilize the traceless property of the Hamiltonian (all the spin-vectors  $F_i$  and spin-tensors  $N_{ij}$  are traceless), which dictates that the sum of the three eigenvalues is zero. For our model (2) with  $\alpha \neq 0$ ,  $H(\mathbf{k}) = k_x F_x + k_y F_y + \alpha k_z (F_z + \gamma N_{ij})$ , here  $\gamma = \beta/\alpha$ . The topological properties would not change by rescaling  $k_z$ . For simplicity, we directly set  $\alpha = 1$  and the integral surface  $\mathbf{S}$  is chosen as the unit sphere with  $k = 1$ . Suppose two bands touch at some specific  $\mathbf{k}$ , at which the three eigenenergies are given by  $E_a, E_a$ , and  $-2E_a$ , then

$$\det(xI - H(\mathbf{k})) = (x - E_a)(x - E_a)(x + 2E_a) = x^3 - 3E_a^2 x + 2E_a^3 \equiv x^3 + d_1 x + d_0, \quad (11)$$

where  $d_1$  and  $d_0$  satisfy  $P(\mathbf{k}) \equiv -d_1^3/27 - d_0^2/4 = 0$ . In the following, we determine the phase transition conditions using  $P(\mathbf{k})$ . If  $P(\mathbf{k})$  cannot be zero, then there is no phase transitions as no level crossings are allowed by tuning parameters. For the 6 spin-tensors, we find the following results (by setting  $y = k_z^2\gamma^2$ ).

(A)  $N_{xx}$ ,  $N_{yy}$ , and  $N_{xy}$  would not induce any band crossing. Consider  $N_{xx}$  as an example.  $P(\mathbf{k}) = k_x^2 y^2 / 27 + (-k_x^4/4 + k_x^2/6 + 1/108)y + 1/27$ . As  $k = 1$ ,  $P(\mathbf{k}) \geq k_x^2 y^2 / 27 + (-k_x^2/4 + k_x^2/6 + k_x^2/108)y + 1/27 = k_x^2 (y - 1)^2 / 27$ . Here “=” is exact for  $|k_x| = 1$ , hence  $y \neq 1$  on the unit sphere  $\mathcal{S}$  and we have  $P(\mathbf{k}) > 0$ . Similarly, we have

$$\begin{aligned} N_{yy}: P(\mathbf{k}) &= k_y^2 y^2 / 27 + (-k_y^4/4 + k_y^2/6 + 1/108)y + 1/27 \geq k_y^2 (y - 1)^2 / 27 > 0; \\ N_{xy}: P(\mathbf{k}) &= y^3 / 1728 + y^2 / 144 - k_x^2 k_y^2 y / 4 + y / 36 + 1/27 \geq y^3 / 1728 + y^2 / 144 - 5y / 144 + 1/27 > 0. \end{aligned}$$

For all the above three cases, the TDP is still type-I.

(B) For  $N_{zz}$ ,  $P(\mathbf{k}) = k_z^2 y^2 / 27 + (-k_z^4/4 + k_z^2/6 + 1/108)y + 1/27 \geq k_z^2 (y - 1)^2 / 27 \geq 0$ . “=” is valid only when  $k_z^2 = 1$  and  $\gamma^2 = 1$ , which is the level-crossing point. Specifically, for  $\gamma = 1$ , the lower (upper) band and middle band touch at  $k_z = 1(-1)$ ; for  $\gamma = -1$ , the upper (lower) band and middle band touch at  $k_z = 1(-1)$ .

(C) For  $N_{xz}$ ,  $P(\mathbf{k}) = y^3 / 1728 + y^2 / 144 - k_x^2 k_z^2 y / 4 + y / 36 + 1/27 \geq y^3 / 1728 + y^2 / 144 - 5y / 144 + 1/27 \geq 0$ . “=” is valid when  $\gamma = \pm 2$  and  $k_x^2 = k_z^2 = 1/2$ . At  $\gamma = 2$ , the lower band and middle band touch at  $\pm k_z = k_x = 1/\sqrt{2}$ . The upper band and middle band touch at  $\pm k_z = -k_x = 1/\sqrt{2}$ . Similar analysis can be applied to another transition point  $\gamma = -2$ . Note that for  $N_{yz}$  the results would be the same, by considering  $k_y \rightarrow k_x$  and  $F_y \rightarrow F_x$ .

(D)  $\alpha = 0$ . In this case,  $H(\mathbf{k}) = k_x F_x + k_y F_y + \beta k_z N_{ij}$ . For  $N_{xx}$ ,  $N_{xy}$ ,  $N_{yy}$ , and  $N_{zz}$ , there exist nodal lines where two bands touch in the band structure (the triply-degenerate node is not the only degenerate point). Thus the Chern number is ill-defined. For  $N_{xz}$  and  $N_{yz}$ , the eigenenergies of  $H(\mathbf{k})$  are given by 0, and  $\pm \sqrt{k_x^2 + k_y^2 + k_z^2 \beta^2 / 4}$ . The band structure is adiabatically connected to the case (C) with  $|\gamma| > 2$ .

As a final remark, the function  $P(\mathbf{k})$  can also be used to determine the splitting of TDPs.

### Splitting of TDPs by a Zeeman term

A small Zeeman term  $\varepsilon F_z$  breaks the triple degeneracy at  $\mathbf{k} = 0$  for type-I and type-II TDPs described by the Hamiltonian (2). As a result, TDPs break into three doubly degenerate Weyl points located at  $W_{\pm} = (0, 0, -\varepsilon/(\alpha \pm \beta))$  and  $W_3 = (0, 0, -\varepsilon/\alpha)$ . Near these three nodes with  $|\delta \mathbf{k}| \ll 1$ , the Hamiltonian reduces to

$$H_{W_+}(\delta \mathbf{k}) = \begin{pmatrix} (\alpha + \beta)\delta k_z & (\delta k_x - i\delta k_y)/\sqrt{2} & 0 \\ (\delta k_x + i\delta k_y)/\sqrt{2} & 0 & (\delta k_x - i\delta k_y)/\sqrt{2} \\ 0 & (\delta k_x + i\delta k_y)/\sqrt{2} & \frac{2\alpha\varepsilon}{\alpha + \beta} \end{pmatrix}, \quad (12)$$

$$H_{W_-}(\delta \mathbf{k}) = \begin{pmatrix} -\frac{2\beta\varepsilon}{\alpha - \beta} & (\delta k_x - i\delta k_y)/\sqrt{2} & 0 \\ (\delta k_x + i\delta k_y)/\sqrt{2} & 0 & (\delta k_x - i\delta k_y)/\sqrt{2} \\ 0 & (\delta k_x + i\delta k_y)/\sqrt{2} & (-\alpha + \beta)\delta k_z \end{pmatrix}, \quad (13)$$

$$H_{W_3}(\delta \mathbf{k}) = \begin{pmatrix} -\frac{\beta\varepsilon}{\alpha} + (\alpha + \beta)\delta k_z & (\delta k_x - i\delta k_y)/\sqrt{2} & 0 \\ (\delta k_x + i\delta k_y)/\sqrt{2} & 0 & (\delta k_x - i\delta k_y)/\sqrt{2} \\ 0 & (\delta k_x + i\delta k_y)/\sqrt{2} & -\frac{\beta\varepsilon}{\alpha} + (-\alpha + \beta)\delta k_z \end{pmatrix}. \quad (14)$$

Therefore the effective two-band Hamiltonians can be expressed as

$$H_{W_+}(\delta \mathbf{k}) = \frac{1}{\sqrt{2}}\delta k_x \sigma_x + \frac{1}{\sqrt{2}}\delta k_y \sigma_y + \frac{\alpha + \beta}{2}\delta k_z \sigma_z + \frac{\alpha + \beta}{2}\delta k_z I_2 + O(\delta k^2), \quad (15)$$

$$H_{W_-}(\delta \mathbf{k}) = \frac{1}{\sqrt{2}}\delta k_x \sigma_x + \frac{1}{\sqrt{2}}\delta k_y \sigma_y + \frac{\alpha - \beta}{2}\delta k_z \sigma_z + \frac{\beta - \alpha}{2}\delta k_z I_2 + O(\delta k^2), \quad (16)$$

up to the linear order of  $\delta \mathbf{k}$  and

$$H_{W_3}(\delta \mathbf{k}) = \alpha \delta k_z \sigma_z - \frac{\alpha}{2\beta\varepsilon}[(\delta k_x^2 - \delta k_y^2)\sigma_x + 2\delta k_x \delta k_y \sigma_y] + (\beta \delta k_z - \frac{\beta\varepsilon}{\alpha})I_2 + O(\delta k^3), \quad (17)$$

up to second order of  $\delta \mathbf{k}$ . The first two are Weyl points with linear dispersions along all three directions, whereas the third one is a multi-Weyl point which has a linear dispersion in the  $k_z$  direction but quadratic dispersion along

the other two directions. The Chern numbers for this multi-Weyl point is  $\mathcal{C} = 2$ . The quadratic dispersion originates from the non-direct (second-order) couplings in  $F_x$  and  $F_y$  between the degenerate energy levels ( $|+1\rangle$  and  $|-1\rangle$ ). For  $|\beta| < |\alpha|$ , the linear Weyl points  $W_{\pm}$  have the same charge  $\mathcal{C} = 1$  ( $\alpha > 0$ ), i.e., the case for type-I TDPs. For  $|\beta| > |\alpha|$ , the linear Weyl points  $W_{\pm}$  have opposite charges  $\mathcal{C} = \pm 1$ , i.e., the case for type-II TDPs.

In the lattice model described by Eq. (3), two TDPs appear at  $(0, 0, \pm \arccos(-\gamma))$ . By adding a Zeeman term  $\varepsilon F_z$ , the TDP at  $(0, 0, \arccos(-\gamma))$  is split into three nodes at  $k_1 = \arccos[-\frac{\varepsilon}{t_0(1+\beta)} - \gamma]$ ,  $k_2 = \arccos[-\frac{\varepsilon}{t_0(1-\beta)} - \gamma]$ , and  $k_3 = \arccos(-\frac{\varepsilon}{t_0} - \gamma)$  along the  $k_x = k_y = 0$  line. Around the first two degenerate nodes, the effective two-band Hamiltonians can be written as

$$H_{k_{1,2}} = \frac{1}{\sqrt{2}}(\delta k_x \sigma_x + \delta k_y \sigma_y) - \frac{t_0 \sin k_{1,2}}{2}(1 \pm \beta)\delta k_z \sigma_z + O(\delta k^2), \quad (18)$$

which describe two linear Weyl points. For  $\gamma = -0.5$ , both Weyl points have  $\mathcal{C} = -1$  for  $0 < \beta < 1$  (type-I) and  $\mathcal{C} = \pm 1$  for  $\beta > 1$  (type-II), which are consistent with our numerical results. The third multi-Weyl point has  $\mathcal{C} = -2$  and can be described by  $H_{k_3} = -t_0 \sin k_3 \delta k_z \sigma_z + O(\delta k^2)$ , whose energy dispersion is linear in the  $k_z$  direction and quadratic in the other two directions. A similar analysis can be applied to the other TDP.

Under the same perturbation, a type-III TDP is broken into four linear Weyl points located at  $(k_x, k_z) = (\pm \beta \varepsilon / (\beta - 2\alpha), 2\varepsilon / (\beta - 2\alpha))$ ,  $(\pm \beta \varepsilon / (\beta + 2\alpha), -2\varepsilon / (\beta + 2\alpha))$  in the  $k_y = 0$  plane. By neglecting those constant terms, the effective two-band Hamiltonians around these Weyl points are given by

$$H_1(\delta \mathbf{k}) = \frac{1}{\sqrt{3}}(\delta k_x - \frac{\beta}{2}\delta k_z)\sigma_x + \frac{1}{\sqrt{3}}\delta k_y \sigma_y - [\frac{1}{3}\delta k_x + (\frac{\beta}{6} - \frac{2\alpha}{3})\delta k_z]\sigma_z + O(\delta k^2), \quad (19)$$

$$H_2(\delta \mathbf{k}) = \frac{1}{\sqrt{3}}(-\delta k_x - \frac{\beta}{2}\delta k_z)\sigma_x - \frac{1}{\sqrt{3}}\delta k_y \sigma_y + [\frac{1}{3}\delta k_x - (\frac{\beta}{6} - \frac{2\alpha}{3})\delta k_z]\sigma_z + O(\delta k^2), \quad (20)$$

$$H_3(\delta \mathbf{k}) = \frac{1}{\sqrt{3}}(\delta k_x + \frac{\beta}{2}\delta k_z)\sigma_x + \frac{1}{\sqrt{3}}\delta k_y \sigma_y - [\frac{1}{3}\delta k_x - (\frac{\beta}{6} + \frac{2\alpha}{3})\delta k_z]\sigma_z + O(\delta k^2), \quad (21)$$

$$H_4(\delta \mathbf{k}) = \frac{1}{\sqrt{3}}(\delta k_x - \frac{\beta}{2}\delta k_z)\sigma_x - \frac{1}{\sqrt{3}}\delta k_y \sigma_y - [\frac{1}{3}\delta k_x + (\frac{\beta}{6} + \frac{2\alpha}{3})\delta k_z]\sigma_z + O(\delta k^2). \quad (22)$$

These four nodal points can be regarded as deformed Weyl points rotated by a spin-tensor  $N_{xz}$  in the  $k_y = 0$  plane.

Although not in the standard form, the four Weyl points are still characterized by the Chern numbers defined in Eq. (1). In principle, the topological invariants can be determined numerically, as we have done. Here, we show that several symmetry arguments can be used for determining their Chern numbers relatively. As the first two Weyl points are related by  $H_1(\delta k_x, \delta k_y, \delta k_z) = H_2(-\delta k_x, -\delta k_y, \delta k_z)$ , they must have the same Chern number. As the last two Weyl points are related by  $H_3(\delta k_x, \delta k_y, \delta k_z) = H_4(\delta k_x, -\delta k_y, -\delta k_z)$ , they must have the same Chern number, too. Note that the four Weyl points always exist even at  $\alpha = 0$  for a finite Zeeman splitting. By tuning  $\alpha$  to 0, they move in the  $k_y = 0$  plane without merging. The entire process is adiabatic because no level touching or crossing occurs.

At  $\alpha = 0$ , as the first and third Weyl points are related by  $H_1(\delta k_x, \delta k_y, \delta k_z) = H_3(\delta k_x, \delta k_y, -\delta k_z)$ , and the first and fourth Weyl points are related by  $H_1(\delta k_x, \delta k_y, \delta k_z) = H_4(\delta k_x, -\delta k_y, \delta k_z)$ , the first two and the last two Weyl points must have opposite Chern numbers. Therefore, a type-III TDP can be split into two pairs of Weyl points with opposite charges, as verified by our numerical results.

### Experimental scheme

Here we discuss how to experimentally realize spin-vector- and spin-tensor-momentum couplings, which are crucial for engineering different types of TDPs. Consider the following three Raman beams

$$\mathbf{E}_{R_1, R_3} = E_{R_1, R_3} e^{\mp i k_m z} [\hat{\mathbf{x}} \cos(2k_0 y) \mp \hat{\mathbf{y}} \cos(2k_0 x)], \quad \mathbf{E}_{R_2} = E_{R_2} e^{i k_1 z} (i \hat{\mathbf{x}} + \hat{\mathbf{y}}).$$

The  $\mathbf{E}_{R_1}$  and  $\mathbf{E}_{R_3}$  fields can be formed by multiple reflections of a beam in a 3D space that is initially polarized along  $\hat{\mathbf{x}}$  and incident in the  $y$ - $z$  plane with an incident angle determined by  $k_1^2 = k_m^2 + 4k_0^2$ . The  $\mathbf{E}_{R_2}$  beam is a traveling wave in the  $z$  direction with a wavevector  $k_1$ . A magnetic field  $\mathbf{B}$  is applied in the  $x$ - $y$  plane with a  $\pi/4$ -angle with respect to  $\hat{\mathbf{x}}$ . The Raman couplings between the hyperfine states are contributed from both  $D_1(6^2S_{1/2} \rightarrow 7^2P_{1/2})$  and  $D_2(6^2S_{1/2} \rightarrow 7^2P_{3/2})$  lines with detunings  $\Delta_{1/2}$  and  $\Delta_{3/2}$ , respectively. The detunings are much larger than the hyperfine structure. The resulting Raman couplings can be obtained by summing over all the transitions allowed by

the selection rules. For the purpose of calculations, we need to decompose the electric field as follows:

$$\begin{aligned} \mathbf{E}_{R_1, R_3} &= \frac{E_{R_1, R_3} e^{\mp i k_m z}}{\sqrt{2}} \{ [\cos(2k_0 y) \mp \cos(2k_0 x)] \hat{\mathbf{B}}_{\parallel} - [\cos(2k_0 y) \pm \cos(2k_0 x)] \hat{\mathbf{B}}_{\perp} \}, \\ \mathbf{E}_{R_2} &= \frac{E_{R_2} e^{i k_1 z}}{\sqrt{2}} [(1+i) \hat{\mathbf{B}}_{\parallel} + (1-i) \hat{\mathbf{B}}_{\perp}]. \end{aligned} \quad (23)$$

The component parallel to (perpendicular to)  $\mathbf{B}$  is used to induce the  $\pi$  ( $\sigma$ ) transition, as illustrated in Fig. 6.

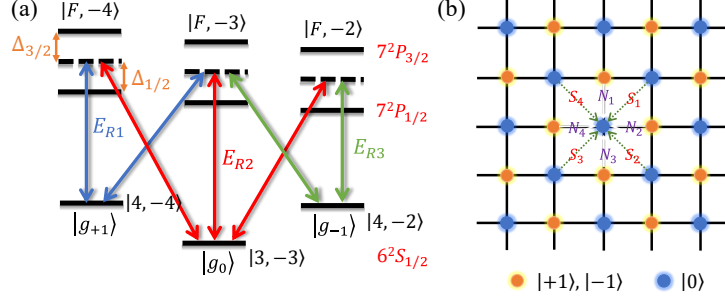


FIG. 6: (a) Optical transitions to generate Raman couplings between three hyperfine states. (b) Schematic of the tight-binding model, in which  $g_{\pm 1}$  stay in one sublattice while  $g_0$  in the other sublattice,  $N_1$  to  $N_4$  denote the nearest-neighbor bonding between different components, and  $S_1$  to  $S_4$  denote the next-nearest-neighbor bonding between the same components.

The Raman coupling between  $g_{+1}$  and  $g_0$  comes from the following two parts by summing over all possible  $F$ :

$$\begin{aligned} M_{+1,0}^1 &= \sum_{J=\frac{1}{2}, \frac{3}{2}}^F \frac{\Omega_{g_{+1}, F, 1\parallel}^{J*} \Omega_{g_0, F, 2-}^J}{\Delta_J} = \frac{\sqrt{7} E_{R_1} E_{R_2} \alpha_{D_1}^2}{12\sqrt{2}} \left( \frac{1}{\Delta_{3/2}} - \frac{1}{\Delta_{1/2}} \right) (1-i) e^{i(k_1+k_m)z} [\cos(2k_0 x) - \cos(2k_0 y)], \\ M_{+1,0}^2 &= \sum_{J=\frac{1}{2}, \frac{3}{2}}^F \frac{\Omega_{g_{+1}, F, 1+}^{J*} \Omega_{g_0, F, 2\parallel}^J}{\Delta_J} = \frac{\sqrt{7} E_{R_1} E_{R_2} \alpha_{D_1}^2}{12\sqrt{2}} \left( \frac{1}{\Delta_{3/2}} - \frac{1}{\Delta_{1/2}} \right) (1+i) e^{i(k_1+k_m)z} [\cos(2k_0 x) + \cos(2k_0 y)]. \end{aligned}$$

Here  $\Omega_{g_s, F, \parallel}^J = e \langle g_s | z | F, 0, J \rangle \hat{e}_z \cdot \mathbf{E}$  and  $\Omega_{g_s, F, \pm}^J = e \langle g_s | e^{\pm} | F, \pm 1, J \rangle \hat{e}_{\pm} \cdot \mathbf{E}$  are the transition matrix elements in the basis of the circularly polarized light in the plane perpendicular to  $\mathbf{B}$ .

Similarly, the Raman coupling between  $g_{-1}$  and  $g_0$  can be written as

$$M_{-1,0}^1 = \sum_{J=\frac{1}{2}, \frac{3}{2}}^F \frac{\Omega_{g_{-1}, F, 3\parallel}^{J*} \Omega_{g_0, F, 2+}^J}{\Delta_J} = \frac{E_{R_2} E_{R_3} \alpha_{D_1}^2}{24\sqrt{2}} \left( \frac{1}{\Delta_{3/2}} - \frac{1}{\Delta_{1/2}} \right) (1-i) e^{i(k_1-k_m)z} [\cos(2k_0 x) + \cos(2k_0 y)], \quad (24)$$

$$M_{-1,0}^2 = \sum_{J=\frac{1}{2}, \frac{3}{2}}^F \frac{\Omega_{g_{-1}, F, 3-}^{J*} \Omega_{g_0, F, 2\parallel}^J}{\Delta_J} = \frac{E_{R_2} E_{R_3} \alpha_{D_1}^2}{24\sqrt{2}} \left( \frac{1}{\Delta_{3/2}} - \frac{1}{\Delta_{1/2}} \right) (1+i) e^{i(k_1-k_m)z} [\cos(2k_0 x) - \cos(2k_0 y)]. \quad (25)$$

It follows that the total Raman couplings between  $g_{\pm 1}$  and  $g_0$  are respectively

$$M_{+1,0} = M_{+1,0}^1 + M_{+1,0}^2 = M_0 e^{i(k_1+k_m)z} [\cos(2k_0 x) + i \cos(2k_0 y)], \quad (26)$$

$$M_{-1,0} = M_{-1,0}^1 + M_{-1,0}^2 = M'_0 e^{i(k_1-k_m)z} [\cos(2k_0 x) - i \cos(2k_0 y)], \quad (27)$$

where  $M_0 = \frac{\sqrt{7} \alpha_{D_1}^2 E_{R_1} E_{R_2}}{6\sqrt{2} \Delta_2}$ ,  $M'_0 = \frac{\alpha_{D_1}^2 E_{R_2} E_{R_3}}{12\sqrt{2} \Delta_2}$ , and  $\frac{1}{\Delta_2} = \frac{1}{\Delta_{3/2}} - \frac{1}{\Delta_{1/2}}$ .

To remove the spatially dependent phase factor in the Raman coupling, we can use the gauge transformation  $U = e^{i(k_1 F_z^2 + k_m F_z)z}$ , which would not affect other terms. In the rotated frame, the Raman coupling then becomes

$$H_R = \lambda k_z (k_1 F_z^2 + k_m F_z) + [\cos(2k_0 x) + i \cos(2k_0 y)] (M_0 |g_{+1}\rangle \langle g_0| + M'_0 |g_0\rangle \langle g_{-1}|) + \text{h.c.} \quad (28)$$

with  $\lambda = \hbar^2/m$  by neglecting those constant term. Since the spin-dependent lattice potentials have the same sign for  $g_{+1}$  and  $g_{-1}$  components, we can write the tight-binding model on a square lattice in the  $x$ - $y$  plane as shown in



Fig. 6(b), in which  $g_{\pm 1}$  stay in one sublattice while  $g_0$  in the other sublattice. We consider the nearest-neighbor and next-nearest-neighbor hopping terms with only  $s$ -orbital of each site. The hopping between the nearest-neighbor sites are between different components induced by the Raman couplings. The hopping between the next-nearest-neighbor sites are between the same component. The effective tight-binding Hamiltonian reads

$$H_{tb} = \frac{\lambda k_z^2}{2} + H_R - \sum_{i,j}^{s=\pm 1,0} t_s c_s^\dagger(\mathbf{r}_i) c_s(\mathbf{r}_i + \mathbf{S}_j) - \sum_i^{s=\pm 1,0} \delta_s c_s^\dagger(\mathbf{r}_i) c_s(\mathbf{r}_i) \quad (29)$$

$$+ \sum_{i,j} t_{so1}^{ij} c_{+1}^\dagger(\mathbf{r}_i) c_0(\mathbf{r}_i + \mathbf{N}_j) + \sum_{i,j} t_{so2}^{ij} c_{-1}^\dagger(\mathbf{r}_i) c_0(\mathbf{r}_i + \mathbf{N}_j) + \text{h.c.}, \quad (30)$$

where the Zeeman term has been incorporated into the detunings in the ground state manifold. The coupling coefficients are

$$t_s = \int d^2\mathbf{r} \phi_s^{i*} \left[ \frac{\lambda}{2}(k_x^2 + k_y^2) + V(\mathbf{r}) \right] \phi_s^j(\mathbf{r}), \quad t_{so1}^{ij} = \int d^2\mathbf{r} \phi_{+1}^{i*} M_{+1,0} \phi_0^j(\mathbf{r}), \quad t_{so2}^{ij} = \int d^2\mathbf{r} \phi_{-1}^{i*} M_{-1,0} \phi_0^j(\mathbf{r}). \quad (31)$$

The spin-flipped hopping coefficients satisfy  $t_{so1}^{jx,jx\pm 1} = \pm t_{so1}$ ,  $t_{so1}^{jy,jy\pm 1} = \pm i t_{so1}$ ,  $t_{so2}^{jx,jx\pm 1} = \pm t_{so2}$ , and  $t_{so2}^{jy,jy\pm 1} = \mp i t_{so2}$ , as constrained by the lattice symmetry. For the spin-dependent lattice, each unit cell contains two lattice sites with primitive vectors along the two diagonal directions (lattice constant  $b = \pi/k_0$ ). Using Fourier transformation and setting  $t_{so1} = t_{so2} = \frac{t_{so}}{2\sqrt{2}}$ , which can be achieved by adjusting the relative strengths of Raman beams, we obtain the following momentum-space Hamiltonian

$$H_{3D}(\mathbf{k}) = \frac{\lambda k_z^2}{2} - 4T_s \cos(k_x a) \cos(k_y a) - \Lambda_s + \lambda k_z (k_1 F_z^2 + k_m F_z) + t_{so} F_x \sin(k_x a) + t_{so} F_y \sin(k_y a). \quad (32)$$

Here  $a = \frac{\pi}{\sqrt{2}k_0}$ , and  $k_x = (k_+ + k_-)/\sqrt{2}$ ,  $k_y = (k_+ - k_-)/\sqrt{2}$  are lattice momenta along  $x$  and  $y$  directions.  $T_s = \text{diag}(t_{+1}, t_0, t_{-1})$  and  $\Lambda_s = \text{diag}(\delta_{+1}, \delta_0, \delta_{-1})$  are diagonal matrices for tunneling and detuning. When  $t_{+1} = t_0 = t_{-1}$  and  $\delta_{+1} = \delta_0 = \delta_{-1}$ , i.e., no Zeeman term, there exist two TDPs in the 2D Brillouin zone spanned by  $(k_x, k_y)$ . They are located at  $(0, 0)$  and  $(\pi, 0)$ . (Note that  $(0, 0)$  and  $(\pi, \pi)$  ( $(\pi, 0)$  and  $(0, \pi)$ ) are the same momenta by folding back to the first Brillouin zone spanned by  $(k_+, k_-)$ ). By expanding the above Hamiltonian around the two points, we obtain the following low-energy Hamiltonians (setting  $a = 1$ )

$$H_1(\delta\mathbf{k}) = \lambda \delta k_z (k_1 F_z^2 + k_m F_z) + t_{so} \delta k_x F_x + t_{so} \delta k_y F_y, \quad (33)$$

$$H_2(\delta\mathbf{k}) = \lambda \delta k_z (k_1 F_z^2 + k_m F_z) - t_{so} \delta k_x F_x + t_{so} \delta k_y F_y, \quad (34)$$

which are similar to the Hamiltonian (2). The two TDPs have the opposite Chern numbers. When  $t_s$  are not equal, the resulting Zeeman field at the two points may be compensated by choosing suitable detuning  $\delta_s$ . In this case, one of two TDPs will survive, whereas the other one will be broken into two Weyl points with opposite Chern numbers.